electronics

Article

A Bicycle-Embedded Electromagnetic Harvester for Providing Energy to Low-Power Electronic Devices

Robert Urbina, Luis Baron, Juan-Pablo Carvajal, Manuel Pérez, Carlos-Ivan Paez-Rueda, Arturo Fajardo*, Germán Yamhure and Gabriel Perilla

Department of Electronic Engineering, Pontificia Universidad Javeriana , Bogota 110311, Colombia; gabriel.perilla@javeriana.edu.co (G.P.)

* Correspondence: fajardoa@javeriana.edu.co

Abstract: Bicycles are rapidly gaining popularity as a sustainable mode of transportation around the world. Furthermore, the smart bicycle paradigm enables increased use through the Internet of Things applications (e.g., GPS tracking systems). This new paradigm introduces energy autonomy as a new challenge. The energy harvesting technology can capture the energy present in the cycling environment (e.g., kinetic or solar) to give this autonomy. The kinetic energy source is more stable and dense in this environment. There are several wheel kinetic harvesters on the market, ranging from low-complexity dynamos used to power bicycle lights to smart harvester systems that harvest kinetic energy while braking and cycling and store it for when it is needed to power sensors and other electronics loads. Perhaps the hub and the "bottle" dynamos are the most commercially successful systems because of their cost-effective design. Furthermore, the bottle generator is very inexpensive, yet it suffers from significant energy losses and is unreliable in wet weather due to mechanical friction and wheel slippage in the wheel/generator contact. This paper proposes a cost-effective bicycle harvester based on a novel kinetic-electromagnetic transducer. The proposed harvester allows for the generation and storage of harnessed kinetic energy to power low-power electronics loads when the user requires it (e.g., cell phone charging, lighting). The proposed harvester is made up of a power processing unit, a battery, and an optimized transducer based on a Halbach magnet array. An extensive full-wave electromagnetic simulation was used to evaluate the proposed transducer. Circuit simulation was also used to validate the proposed power unit. The proposed harvester generates a simulated output power of 1.17 W with a power processing unit efficiency of 45.6% under a constant bicycle velocity of 30 km/h.

Keywords: electromagnetics; transducers; power conversion; circuit simulation; magnetic circuits; energy harvester

Citation: Urbina, R.; Baron, L.; Carvajal, J.-P.; Pérez, M.; Paez-Rueda, C.-I.; Fajardo, A.; Yamhure, G.; Perilla, G. A Bicycle-Embedded Electromagnetic Harvester for Providing Energy to Low-Power Electronic Devices. *Electronics* **2023**, *12*, 2787. https://doi.org/10.3390/electronics12132787

Academic Editors: Noel Rodriguez, Moshe Averbukh and Shailendra Rajput

Received: 20 March 2023
Revised: 22 May 2023
Accepted: 23 May 2023
Published: 24 June 2023

1. Introduction

Megacities around the world are currently grappling with complex issues such as mobility, pollution, and resource sustainability [1]. Urban mobility, in particular, is a major issue that affects almost all of the major cities [2]. Other undesirable effects of inefficient mobility in large cities are related to public health concerns [3]. One of the most promising trends in addressing this issue is the use of alternative transportation methods rather than traditional vehicles, which allows for lower pollution and better air quality in cities [1]. Recently, the use of bikes for short-distance routes has been boosted by city governments building bike paths, lowering taxes, and so on [4]. Despite the availability of appropriate infrastructure, many citizens do not use bicycles as a mode of transportation. In this scenario, the concept of "smart cycling" enables a shift in the perception of bicycles as an important part of the urban technological ecosystem by improving cyclists' experience and safety [5,6]. This paradigm is going to encounter numerous political, economic, and technological challenges. In [1], the authors identify three major research technological trends: smartphone-based cycling (i.e., route planning, delivery services, bike sharing), IoT-bikes (i.e., sustainability and environmental monitoring, promoting health through connected bikes, the Internet of Bikes), and connected e-bikes (i.e., the e-bike market). These applications are supported in a variety of electronic devices (i.e., cell phones, sensors, and lights) that use batteries as an energy source. The widespread use of batteries may harm the environment [7]. The key technology to provide green energy to the low-power electrical components embedded in public transportation is the energy harvesting (EH) technique [8], which can power electrical loads using the energy sources present in the operating environment [9–11]. A generic EH harvester is composed of an environmental energy source, a transducer, and an electrical power processing unit (PPU), as illustrated in Figure 1.

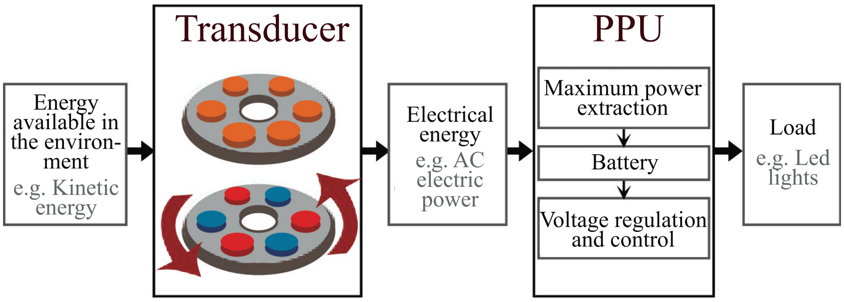

Figure 1. Diagram of an electromagnetic harvester.

The transducer converts environmental energy into electrical energy, which the PPU then conditions and manages for the load. In general, EH systems can be divided into two architectures: those without storage capacity and those with storage capacity [12,13]. In the first approach, the energy is collected by the harvester and immediately supplied to the electric load (e.g., bottle dynamo). In the second, the PPU stores (all or a portion of) the collected energy in order to provide uninterrupted power to its electric load in the future. As a result, under energy neutral operation, the harvester with storage capacity can continuously power the electric device using the environmental energy source. The design goals for achieving this energy autonomy are as follows [9,12,14]: (1) The transducer's energy conversion efficiency must be maximized. (2) The PPU must be able to extract the maximum amount of energy from the harvester. (3) The PPU stores, processes, and delivers electricity to the load without loss. The PPU ensures energy neutral operation, which means that the energy consumed by the payload must always be less than or equal to the ambient energy converted into electrical energy by the harvester.

Mechanical, wind, wave, geothermal, and solar energies are all present in some environments and can be used to generate clean electric energy sources using EH [14]. In the bicycle environment, however, mechanical energy is the source with the highest energy density. The mechanical EH can be separated into three categories: electromagnetic EH, piezoelectric EH, and friction EH [10]. In the piezoelectric EH, the harvester generates electric power from kinetic energy in the environment (e.g., the weaving movement in bicycle riding) using piezoelectric materials. Several authors have researched this EH method in the bicycle context [15–18]. In the friction EH, using a transducer (e.g., a triboelectric generator), the harvester generates electric power from friction between surfaces in the environment, such as the friction produced by the bicycle breaking. This EH approach has been researched recently in the bicycle scenario [19–21]. In the electromagnetic (EM) EH, a harvester produces electric energy from the kinetic energy present in the environment using an EM transducer. The EMEH in the land transportation environment was focused on the harvesting of the kinetic energy present in the movements of the wheels [22]. Furthermore, this kinetic energy source is the one with the highest energy density in the bicycle's environment [23,24]. In addition, to improve the efficiency of the EM harvester, friction, electromagnetic, and electrical losses must be reduced. The friction losses are caused by the contact between the harvester and the wheel, while the electromagnetic losses are caused by the required separation between the stationary and rotational parts of the magnetics device (e.g., the air gap between the stator and rotor of the dynamo). Finally, electrical losses are associated with energy losses caused by heat dissipation of the electric and electronic components involved in power processing. The resulting energy flow is shown in Figure 2a.

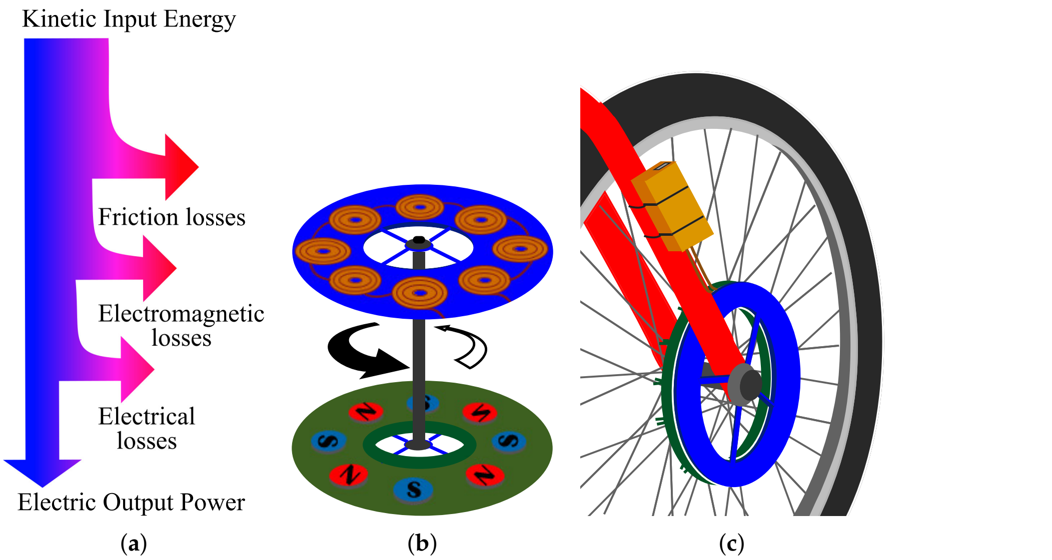

Figure 2. Electromagnetic-hub transduced based on a magnet and coil disks. (**a**) A harvester's generic energy flow based on an electromagnetic transducer. (**b**) Transducer topology detail. (**c**) Standard mounting on a bicycle wheel.

Since the "bottle" dynamo in the 1940s, the concept of EMEH has been popular [25]. During the 1950s, friction-less hub generators at the wheel/generator interface appeared as an improvement, and they were reliable in wet weather [26]. However, it was only in the twenty-first century that it became efficient enough to generate a few watts at a moderate bicycle speed [25,27]. Furthermore, in [26], the author suggests stacking multi-pole dynamos to increase efficiency even further. The concept of an EMEH based on a "bootle" dynamo as a transducer with energy storage capacity was proposed in a pioneering work published in 1991 [28]. Furthermore, this approach has been revisited in some recent works that used hub generators and/or bottle dynamos as transducers [29–31]. These works concentrated on the solution's functionality rather than the harvester optimization (i.e., the transducer or PPU's). The reported generating power was in the units of Watts range at moderate bicycle speeds (between 10 and 30 km per hour). Furthermore, the authors do not analyze the mechanical-electrical efficiency of the harvester, which is a significant drawback. This is because if the efficiency is low, people will experience noticeable resistance when riding bicycle.

In 2009, MIT's Senseable City Lab, in partnership with the city of Copenhagen, developed the Copenhagen Wheel (from harvester to ebike jump). It is based on a brushless motor, advanced sensors, control systems, and a lithium-ion battery, all enclosed within the rear wheel hub [32]. However, it has not achieved commercial success, possibly due to its high cost [32]. Recently, hybrid EH systems have been proposed as a cost-effective alternative to conventional dynamos. These systems generate electricity from multiple EH energy sources [10,23]. In [23], a hybridized nanogenerator based on EM, triboelectric, and thermoelectric generators was presented. Using the generators, the resulting hybrid energy harvester collects all of the energy sources from the relative rotational motions of two disks. The prototyped harvester is a 15 cm diameter disk that can achieve a constant voltage of 5 V and a maximum current peak of 160mA (i.e., 0.8 W) at 3000 rpm (i.e., approximately 80 km/h). In [10], the author proposes a rotational kinetic energy harvester that makes use of a magnet array to deform a piezoelectric sheet and harvest the wheel's kinetic energy. The resulting harvester is a 15 cm diameter disk with a power peak of 10.07 mW at 160 rpm (roughly 5 km/h). The EM harvesters involved in these two works are built on rotating magnet arrays and stationary coils that convert the rotary motion into an induced voltage, as shown in Figure 2. Because this magnetic topology generates flux lines in all directions, it is necessary for at least two windings to capture all of the flux created by the rotating magnet array in order to convert this energy. Consequently, a topology with only a one-sided coil array exhibits low efficiency, which could partially explain the low power contribution of the EM energy source in the proposed hybrid harvesters.

The Halbach array is a type of magnetic array that produces a strong and focused magnetic field on one side while reducing it on the other. Several researchers have investigated its impact on the design of EM energy harvesters in recent years [33–39]. The results of these studies show that energy harvesters using Halbach arrays outperform traditional EM systems in terms of power output and conversion efficiency.

This paper proposes a cost-effective EM harvester that utilizes a non-contact energy harvesting method. It is less affected by weather and ambient temperature and does not require modification of the original bicycle structure for installation. Furthermore, to increase efficiency, reduce mechanical resistance, and enhance the riding experience, various magnet arrays, including Halbach arrays, were systematically tested using full-wave and co-circuit simulations. The electromagnetic simulation was carried out using Ansys Maxwell® software Available online: https://www.ansys.com/products/electronics/ansys-maxwell (accessed on 21 May 2023), based on finite element analysis, and the circuit simulation was performed using Pspice ORCAD® software Available online: https://www.orcad.com/ (accessed on 21 May 2023) . The simulated results demonstrate that under constant speed conditions of 30 km/h (as many city cyclists travel at speeds of up to 50 km/h and rarely slower than 15 km/h [25]), the proposed harvester can generate a constant power of 1.17 W with an PPU efficiency of 45.6 percent. This power output can be utilized to power low-power devices such as WSN network nodes [12]. The rest of this article is organized as follows: Section 2 examines the overall characteristics of the proposed harvester. Section 3 describes the harvester design and validation process. Section 4 discusses the results, while Section 5 summarizes the main conclusions and future work.

2. Proposed Harvester

2.1. Transducer Topology

As shown in Figure 2, the transducer is made up of two disks that seek to be connected between the wheel and the forks of the bicycle frame. The first disk is made up of windings and must be attached to the bicycle's handlebar, while the second disk is made up of magnets and must be attached to the wheel in such a way that the magnet disk spins on the coil disk while the cyclist advances (see Figure 2). Certain harvester dimensions must match those of a standard bicycle with a front brake in order to be easily used and thus reduce the cost involved. Table 1 summarizes the transducer and harvester conditions.

Table 1. Electromagnetic transducer dimensions and external conditions imposed on the harvester design.

Transducer Dimension	Value	Harvester Consideration Parameters	Value
Maximum outer radius	16 cm	Magnet-winding distance separation	5 mm
Minimum inner radius	5 cm	Rim radius	35.35 cm
Maximum height	2 cm	Rotation speed	225 rpm

2.2. Magnets Configuration

The voltage induced on the winding is given in (1) using the Lenz equation. Increasing the magnetic flux (ϕ_B) or increasing the flux variation ($d\phi_B/dt$) increases the voltage induced on a winding (ξ). On one hand, the rotation speed of the magnets can be raised to increase flux variation. However, in this study, this term is linked to the user's pedaling capacity and is treated as a constant parameter. On the other hand, increasing the winding area (A), increasing the magnetic flux density (B), or adjusting the incidence angle (i.e., $\cos(\theta)$) of the fieldlines flowing through the winding region can all enhance the magnetic flux.

$$\xi = -\frac{d\phi_B}{dt}, \phi_B = B \cdot A \cdot \cos(\theta) \tag{1}$$

The goal of this work is to increase the magnetic flux by using magnet configurations, as shown in Figure 3. The field lines are oriented in a single direction in a unidirectional arrangement (see Figure 3a), resulting in low flow variation. The field lines in a north–south–north (NSN) magnet setup (see Figure 3b) are orientated in the opposite direction, resulting in flux fluctuation but reduced magnetic flux density. In comparison to an NSN array, the Halbach magnet array (HAL) generates a flux fluctuation (see Figure 3c), which causes the magnetic field to be focused (e.g., downwards). As a result, HAL configurations allow an EM induced voltage on the windings to be increased.

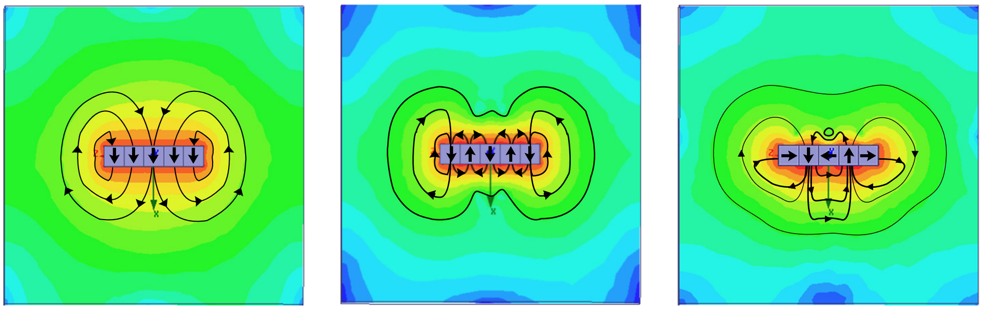

(**a**) (**b**) (**c**)

Figure 3. Magnetic field radiated by permanent magnets modified for illustration purposes from a FEM simulation in which the colors correspond to magnetic field magnitude (i.e., red to blue implies higher to lower magnetic field values). (**a**) Unidirectional Arrangement. (**b**) North–south–north arrangement. (**c**) Halbach arrangement.

2.3. Parametric Analysis of Transducer Variables

Figure 4 shows the various degrees of freedom probed in the transducer's parametric design. The coil was divided into an even number of circular planar windings that are connected in opposite phase; the diameter of the windings D_b is chosen so that it occupies the area of two magnets, in order to benefit from the maximum change in magnetic flux produced by the magnets. The following variables were considered in the design (assisted by computer) of the coil disk: the number of turns and size of each planar coil, the gauge of the wire, and the material from which it is made. Following parametric sweeps of the coil disk variables, some insights were: A greater number of turns for each coil increases the flux variation due to an increase in transversal area and, thus, the induced voltage; additionally, increasing the number of turns increases the length of the wire, which affects the resistance of the coil and its quality factor, lowering the current through it. When the wire's gauge is increased, the same effects occur. Finally, magnets with a larger surface area are more effective at increasing power generation than magnets with a higher height. Parameters such as the shape, quantity, orientation, material, and magnetization grade of the magnets were considered when designing the magnet disk.

The parametric simulation results of these variables show that the greater the number of magnets, the greater the amount of electrical energy collected.NdFeB magnets were used for the transducer because of their hardness, high magnetization, and low cost [40,41]. NSN and HAL array orientations were also used. Furthermore, it was found that the voltage induced on a coil decreases as one moves away from the magnets. Furthermore, the generated energy decayed when the angle of incidence of the magnetic field lines was tilted on each flat coil, for which the perpendicular orientation of the field to the windings was maintained in all simulated prototypes. It should be noted that the power delivered by the transducer is directly proportional to the efficiency of the PPU. An equivalent circuit model is extracted from the transducer, allowing the UPP design to be evaluated in order to extract the most power.

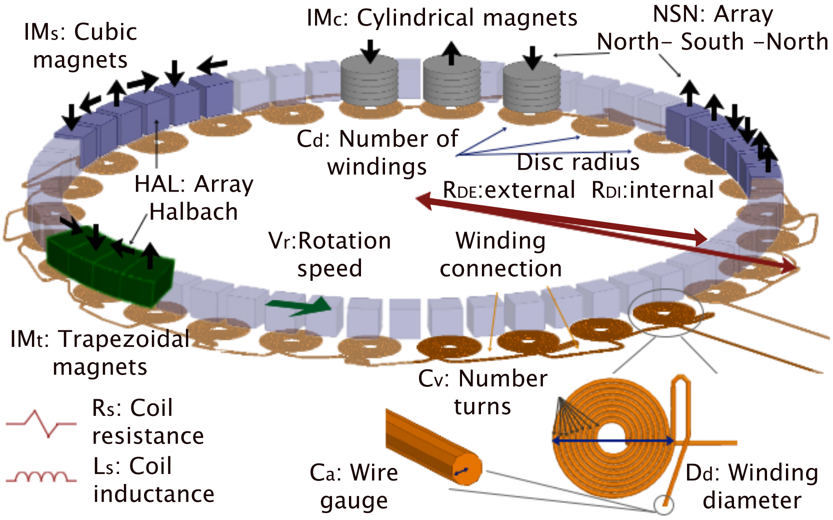

Figure 4. Design parameters of the electromagnetic transducer.

2.4. PPU Design

A full-wave diode bridge, a ripple smoothing filter, and two boost converters constitute the proposed PPU. The transducer output voltage is increased by Boost A to charge the battery (i.e., 3.7 V Li-ion), and Boost B is powered by the battery to drive the 5 V load. This topology is shown in Figure 5. The schematic of the simulated PPU is depicted in Figure6a. As shown in Figure 6b, a full-wave diode bridge and filter were employed to correct the transducer's AC signal and reduce ripple. Due to their low turn-on voltage ($V_{gamma} = 0.3$ V), MBRS410LT3 Schottky type diodes were utilized to rectify the signal [42]. Every inductor and capacitor was modeled using commercial values and their corresponding ESR. Figure 6b also shows the Boost A converter, which was designed to switch at a frequency of 33 kHz, with a SIA414DJ reference mosfet with low on-resistance ($R_{on} = 13$ mΩ). The converter's pulse with modulator circuit is depicted in Figure 6c, and it employs AD8041 reference operational amplifiers because of its rail-to-rail construction and 160 V/µs slew rate characteristics [43]. The converter Boost B design in Figure 6d, was taken from the application note of the TPS61288 fully-integrated synchronous boost converter [44], which already includes a 5 V DC voltage regulator with a typical commutation frequency of 600 kHz. A voltage source, a parasitic resistance (R_{ds}), which represents the cathode conduction losses, and a parallel resistance (R_{ad}), which represents the self-discharge losses made up the battery model that was proposed in the simulation, as illustrated in Figure 6a. Finally, the efficiency of the PPU was improved in this work by designing a Boost A converter with discrete components to research the performance of energy extraction with a control loop that allows the duty cycle of the converter to be varied while maintaining a constant impedance as a load to the transducer (i.e., maximum power point tracking approach).

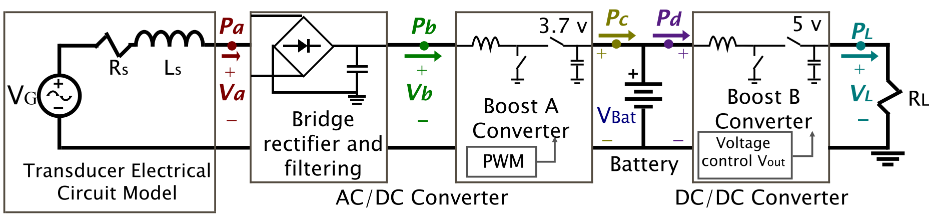

Figure 5. Schematic circuit of the proposed PPU.

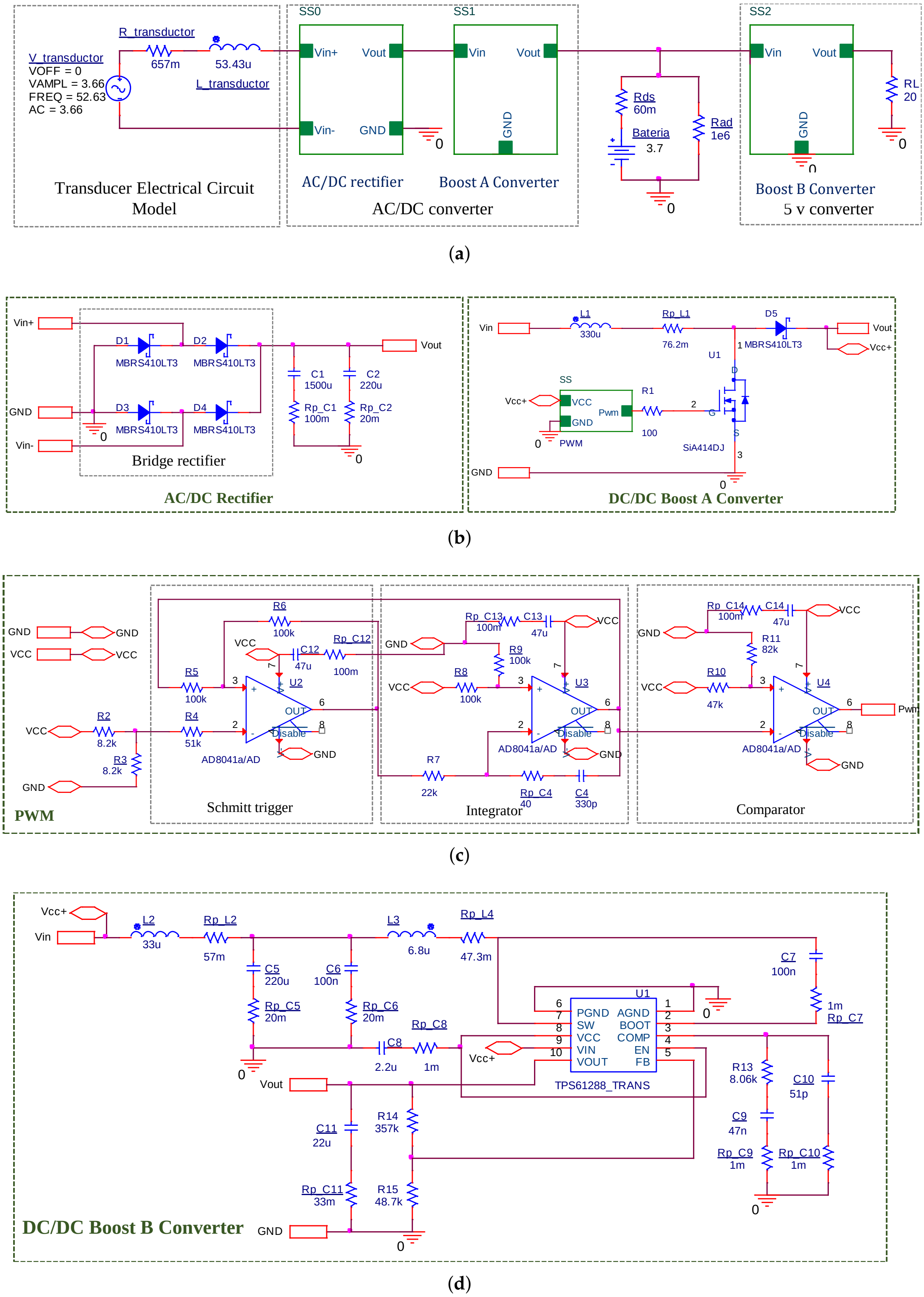

Figure 6. Schematic diagram of the simulated PPU in OrCAD. (**a**) General circuit connection with battery model. (**b**) AC/DC rectifier and Boost A. (**c**) Pulse with modulator used in Boost A. (**d**) Boost B.

3. Design and Validation Methodology

The conditions that the harvester must meet in order to be coupled to a bicycle wheel were first determined for design and validation. To optimize the harvester, full-wave electromagnetic simulation of the transducer based on finite element analysis using the finite element method was carried out using Ansys Maxwell® software. Finally, a lumped circuit was used to model the optimized transducer (see Figure 6a), which was then used to guide the simulation of the proposed PPU and later its validation using Pspice ORCAD® software).

3.1. Transducer Simulation Setup

As shown in Figure 7, the 3D topology was implemented in the Ansys Maxwell® interface, and the EM transducer was simulated using the Magnetic Transient Solver. This solver computes instantaneous magnetic fields at each time step. Each topology's transducer was simulated using 266 ms of simulation time, with time steps of 0.5 ms. As a source, we employ moving permanent magnets. We set the mesh to obtain enough accuracy because this solver does not use adaptive mesh refinement. The equations solved in this approach are [45]:

$$\nabla \times \frac{1}{\sigma}\nabla \times H = -\frac{\partial H}{\partial t}; \nabla \cdot H = 0 \tag{2}$$

To set up the sources, the magnet's physical properties were set using the parameters listed in Table 2. Furthermore, three-dimensional unit vectors are used to represent the magnetic field's orientation. Knowing that the direction of each magnet on the x-y plane can be denoted by cylindrical parameterization, as expressed in (3).

$$\begin{aligned} \hat{x} &= \pm\, Cos\left(\frac{2\pi N_i}{N}\right) \\ \hat{y} &= \pm\, Sin\left(\frac{2\pi N_i}{N}\right) \end{aligned} \tag{3}$$

where N_i is the magnet's position number and N is the total number of magnets. In the magnetization direction, the sign of sinusoidal operations is chosen for convenience. Depending on the position of the magnet, the $\hat{z}$-direction was assigned as either positive ornegative.

Table 2. NdFeB configuration in simulation.

Parameter	Value	Units
Relative Permeability	1.05	
Magnitude	836[a]	kA/m
	796[b]	kA/m
Bulk Conductivity	667	$k\Omega^{-1}/m$
Mass Density	7500	kg/m^3
Core Loss Model	None	w/m^3
Composition	Solid	

[a] For N48 grade magnets. [b] For N52 grade magnets.

An additional geometric structure must be created that completely covers the volume of the magnets without intercepting the coil; this structure is referred to as the movement band with air properties. The magnets' rotation movement is configured on the motion band as shown in Table 3. A simulation region, which is a cube that covers the entire transducer model (see Figure 7), was also created with air properties. A simulation sweep was performed to determine the dimension of the cube, with the length side being varied from a maximum value of 2 m and reduced until convergence with a length of 50 cm.

The simulation model of the coil was built using boolean operations on multiple solids, yielding a 3D solid of a cylinder that starts right at the edge of the simulation region, then curves to generate the respective windings. To assign the two connection ports to the external circuit, the coil must end at the edge of the simulation region. Table 4 displays the common coil parameters set for all topologies. To determine the maximum available power of the transducer, we used co-simulation between the circuit simulator and the FEM simulator. To achieve maximum power, an external circuit was created in Ansys' circuit editor and then imported as a Netlist file into Ansys Maxwell.

Table 3. Motion band setup.

Parameter	Value
Movement	Rotational
Rotation axis	z
Mechanical transient	Deactivated
Initial position angle	0°
Rotation speed	225 rpm

Table 4. Configuration for the coil disk.

Parameter	Value
Material	Copper
Mesh grid	1000
Terminals	CoilTerminals

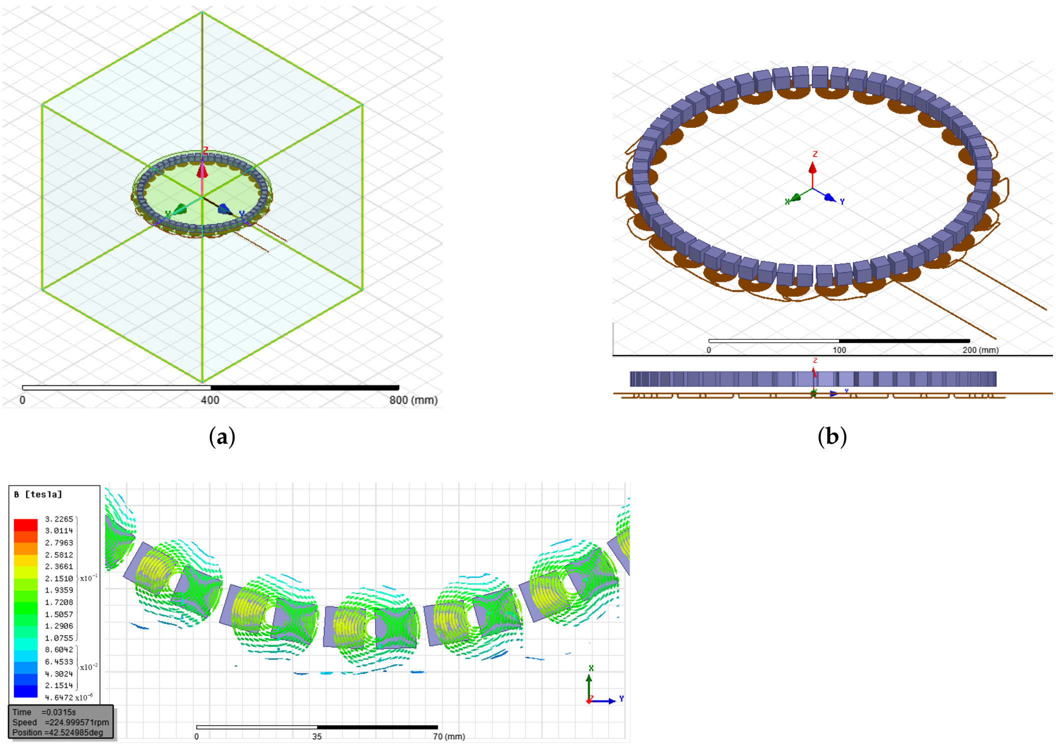

(**a**) (**b**)

(**c**)

Figure 7. Simulation views. (**a**) Simulation region. (**b**) Top and side view of the transducer. (**c**) Magnetic fields on the coil.

3.2. Transducer Evaluation Methodology

The degrees of freedom to be analyzed in the transducer design were selected, and 9 topologies were defined and simulated. The simulation results and the following figure of merit (FMT) were used to select the best transducer for this application:

$$F_{nMT} = \frac{1}{3}\left(\frac{V_{nGp}}{I_{nGp} max\left(\frac{V_{Gp}}{I_{Gp}}\right)} + \left(1 - \frac{C_{nT}}{max(C_T)}\right) + \frac{P_{nL}}{max(P_L)}\right) \quad (4)$$

where F_{nMT} is the computed figure of merit for transducer n, V_{Gp} is the generated peak voltage, I_{Gp} is the peak current through the circuit at maximum power extraction, C_T is the magnets' total cost, and P_L is the average power provided by the transducer. $max(x)$ denotes the maximum value of a given parameter. This figure of merit permits analyzing the convenience in the design of the PPU through the V_{GP}/I_{GP} ratio, the implementation cost, and the transducer's generated power, all with the same percentage value in the final value.

The transducer was designed using magnetic transient simulations in the FEM software. Considering the degree of magnetization and orientation of neodymium magnets changes depending on the array layout, various set-ups were simulated, as illustrated in Figure 8.

3.2.1. Proposed Topologies

Nine alternative transducer topologies have been simulated. Table 5 presents the geometrical characteristics of each topology (see Figure 4). Figure 8 also displays a 3D representation of the generated topologies.

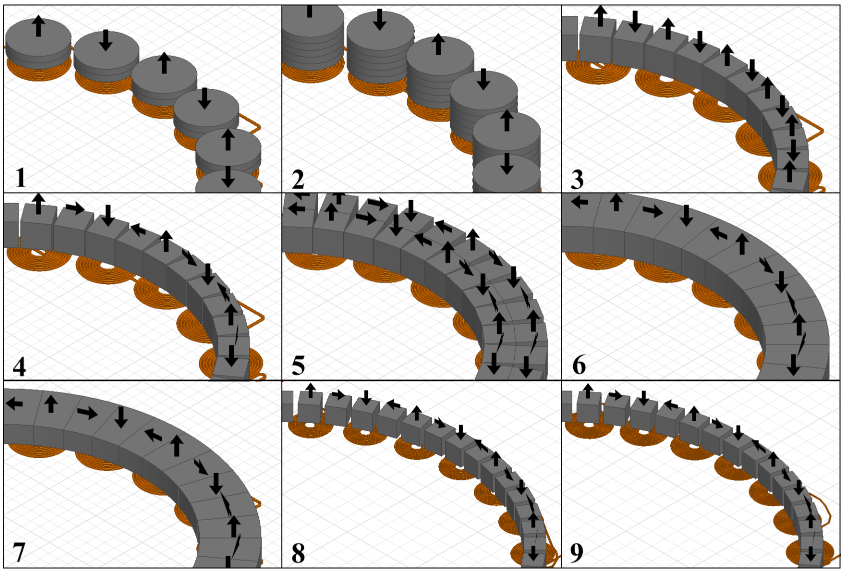

Figure 8. 3D modeling of the different topologies for the transducer. Table 5 summarizes the description of each array.

Table 5. Characteristics of electromagnetic transducers.

ID	R_{DI} [cm]	R_{DE} [cm]	C_d	D_d [cm]	C_a (1)	N_v	Magnets Shape	Grade	Array	Magnets Number
1	6.9	10.3	20	2.7	18	8	Cylindrical magnet (2)	N52	NSN	40
2	6.9	10.3	20	2.7	18	8	Cylindrical magnet	N52	NSN	100
3	6.9	10.3	20	2.7	18	8	Cubical magnet (3)	N48	NSN	40
4	6.9	10.3	20	2.7	18	8	Cubical magnet	N48	HAL	40
5	6.9	10.3	20	2.7	18	8	Cubical magnet	N52	HAL	80
6	6.9	10.3	20	2.7	18	8	Trapezoidal magnet (4)	N52	HAL	40
7	6.9	10.3	20	2.7	18	8	Trapezoidal magnet (5)	N52	HAL	40
8	11.9	15.3	28	2.5	18	8	Cubical magnet	N48	HAL	56
9	11.9	15.3	28	2.7	20	11	Cubical magnet	N48	HAL	56

(1) AWG standard. (2) Cylindrical magnet: Radius 12.5 mm × Heigth 3 mm. (3) Cubical magnet: 12 mm side. (4) Trapezoidal magnet 1: Angle 9° × Radius 25 mm × Heigth 12 mm. (5) Trapezoidal magnet 2: Angle 9° × Radius 25 mm × Heigth 9 mm.

3.2.2. Circuit Model of the Transducer

The initial transducer circuit model is shown in Figure 5, where V_G stands for the induced voltage on the coil, R_s is the coil resistance, L_s is the coil inductance and R_L is the transducer load resistance.

The values of R_s and L_s are initially computed in the static regime (i.e., magnets without movement). For that, the 3D coil model is simulated by connecting the external circuit with an external DC voltage test source. Then from the simulation results R_s y L_s are obtained through the Equation (5).

$$R_s = \frac{V_p}{I_{max}}, L_s = \frac{F_{max}}{I_{max}} \tag{5}$$

where V_p is the DC voltage test source, I_{max} is the flowing current value and F_{max} is the magnetic flux once the transient is finished.

For determining the values of R_s and L_s in the dynamic regime (i.e., magnets in movement), simulations are performed by first, connecting the external circuit to a load resistance of $R_{L1} = 100$ kΩ which allows to estimate voltage V_G in open circuit, which is taken as a null phase shift reference $|\vec{V}|\angle 0$. Then, the circuit is simulated with a resistance load $R_{L2} = R_s$, where R_s is the resistance found in the static regime. Finally, by taken the values of the signal frequency ω, the magnitude and phase shift angle of the current $|\vec{I}|\angle\phi$ obtained from the simulation results, the values of R_s y L_s in the dynamic regime are computed through the Equation (6).

$$\begin{aligned} R_s &= \Re\left\{\frac{|\vec{V}|\angle 0}{|\vec{I}|\angle\phi} - R_{L2}\right\} \\ \omega L_s &= \Im\left\{\frac{|\vec{V}|\angle 0}{|\vec{I}|\angle\phi} - R_{L2}\right\} \end{aligned} \tag{6}$$

Because the values of R_s y L_s in the static and dynamic regimes are so close, only the ones in the dynamic regime are used in the transducer's electric circuit model. Power factor correction was not carried out in the PPU since it had no significant impact on the power extraction of the transducer and was therefore left out of the power management.

3.3. Harvester Simulation Setup in the Circuit Simulator

The circuit model of the chosen transducer was used to simulate the proposed Harvester (transducer and PPU) in Pspice ORCAD ® software. We use transient simulation with all of the storage electric element's initial conditions set to zero. This method computes a circuit's response (solves the Kirchhoff laws) over a time interval specified by the user. Internal time steps affect the accuracy of the transient analysis. We use solver 1 with a maximum time step of 1 s and a final simulation time ranging from 40 to 200 ms [46].

4. Analysis Results

This section reports the results of the nine transducer topologies that were examined. Furthermore discussed are the performance indicators and design objectives for choosing the transducer. The outcomes are also shown when the PPU simulation is employed. The performance metrics and the design goals for the transducer selection are also presented. When the PPU simulation is used, the results are also displayed.

4.1. Simulated Results of the Transducer

Table 6 shows the voltage and current simulation results of the different transducer topologies with different circuit values of resistance R_S, inductance L_S, magnets cost and the obtained values of the figure of merit. For the power generated by the transducers, $R_L = R_s$ was chosen as the load resistance because it best approximates maximum power extraction while ignoring the phase shift caused by the inductance.

Table 6. Simulation results of the electromagnetic transducers.

ID	R_s $[m\Omega]$	L_s $[\mu H]$	C_T [a] [€]	V_{Gp} [V]	I_{Gp} $[A]$	f $[Hz]$	Power $[W]$	F_{MT}
1	196	20	74	1.13	2.88	37.54	1.04	0.478
2	196	20	170	1.62	4.16	37.54	2.19	0.511
3	196	20	108	1.12	2.85	38.46	0.74	0.416
4	196	20	108	1.26	3.23	38.46	1.04	0.450
5	196	20	176	1.92	4.89	38.46	2.39	0.520
6	196	20	340	2.12	5.42	38.46	2.99	0.434
7	196	20	340	1.72	4.39	37.54	2.65	0.397
8	281	26	134.4	2.35	4.17	52.63	2.54	0.630
9	657	53.4	134.4	3.66	2.81	52.63	2.58	0.830

[a] Taken from [41].

According to the figure of merit results, the transducer of case 9 was the one that best adapted to the previously described criteria, so it was chosen as the final transducer to be circuitly simulated alongside the PPU. Figure 7 shows the 3D model of the final version of the transducer, which met the dimensions specified in Table 1. The proposed design consists of 28 flat coils interconnected in a push-pull pattern with 20 gauge copper wire and N48 grade NdFeB magnets in Halbach configuration. Figure 9 depicts the final transducer signals obtained through simulation. The fast Fourier transform (FFT) of the transducer signal confirms that there is little harmonic interference and that the main frequency is 52.63 Hz. To evaluate the circuit model of the selected transducer, in Figure 10, we compare the current and voltage signals generated by the circuit simulation of the transducer model and the simulation by finite element analysis of the 3D model of the transducer. The resulting mean absolute percentage error between the two models was 3.02%.

4.2. Simulated Results Of the Harvester

The PPU was simulated in OrCAD using the final transducer model obtained from the electromagnetic simulations. The induced voltage signal in the transducer V_G was obtained from the Ansys model's simulation result of the open circuit.

The performance of the Boost A converter with a variable duty cycle was examined, and it was revealed that the control consumed more energy than was gained from the improvement. As a result, the usable cycle of the converter was set at a constant value of 63%. To determine the harvester's efficiency and maximum power generated, the load at the output of the Boost B (see Figure 6d) converter was varied until the lowest load caused zero average power in the voltage source of the battery model. According to the aforementioned, the harvester can power a 21.3 Ω load without using battery power. The voltage signals in different nodes (named in Figure 5) of the PPU are shown in Figure 11. When rectifying the voltage signal, the efficiency of the diode bridge was compromised due to the low magnitude of the induced voltage. Furthermore, because the voltage after the bridge rectifier had a ripple of nearly 1 V, the efficiency of Boost A is affected. The maximum voltage ripple was 100 mV for the battery model and 264 mV for the harvester load. Finally, Figure 12 depicts the efficiency of the power chain at various stages of the PPU, following the notation of Figure 5. The efficiency of the converter between stages was calculated using the steady-state current and voltage signals via Equation (7).

$$\eta_p = \frac{1/T \int_0^T V_{out}(t) \cdot I_{out}(t)\, dt}{1/T \int_0^T V_{in}(t) \cdot I_{in}(t)\, dt} \cdot 100\% \tag{7}$$

The PPU was able to extract 81.1% of the maximum power that the transducer could produce, according to the efficiency results presented in Figure 12. The rectifier bridge was the stage that lost the most power, while the integrated Boost B converter was the most efficient. The PPU's overall efficiency was 45.6%. The harvester, which was attached to a bicycle wheel moving at 30 km/h, produced 1172 W for the load. In Figure 13, it can be seen that the output voltage is independently regulated if the current is produced by the transducer and/or provided by the battery.

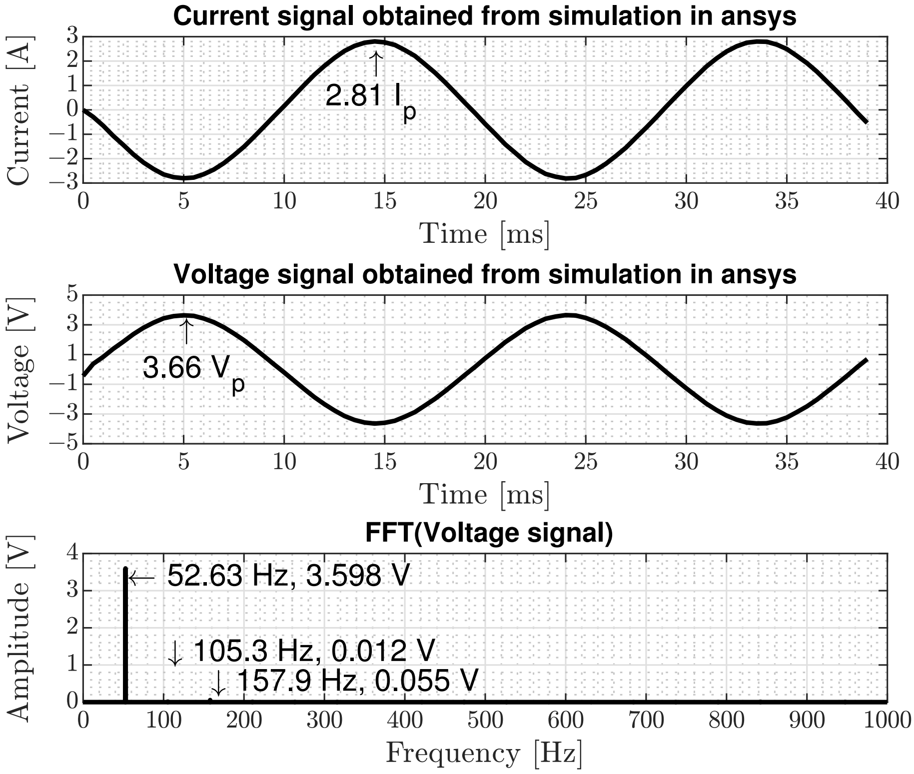

Figure 9. Simulation results for the selected transducer.

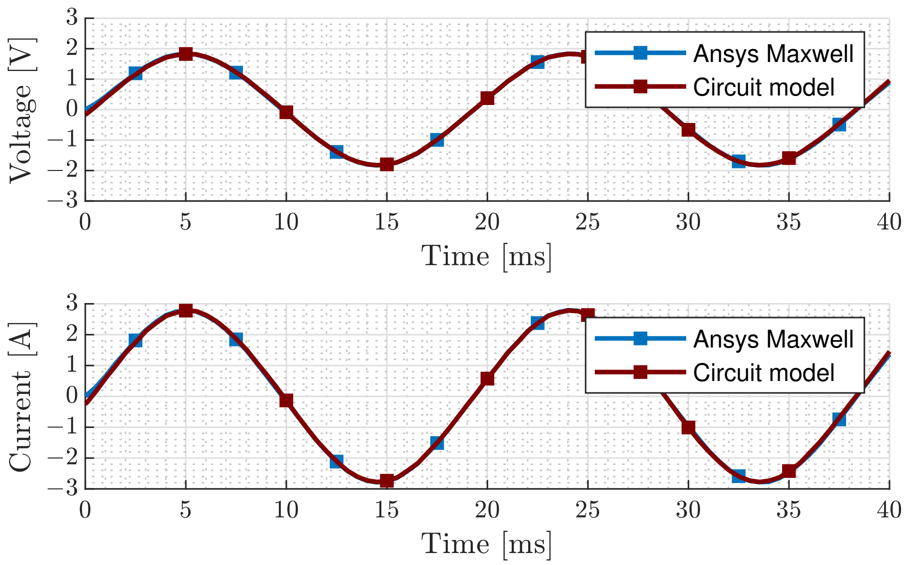

Figure 10. Current voltage signals of the selected transducer with a resistive load $R_L = 657\ \text{m}\Omega$.

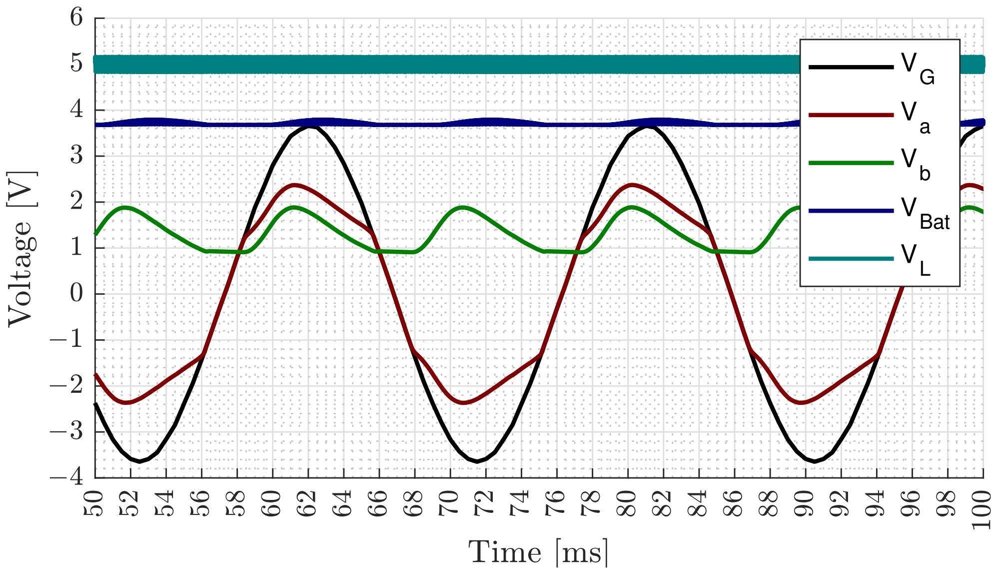

Figure 11. Voltage in the stages of the simulated PPU (see Figure 5).

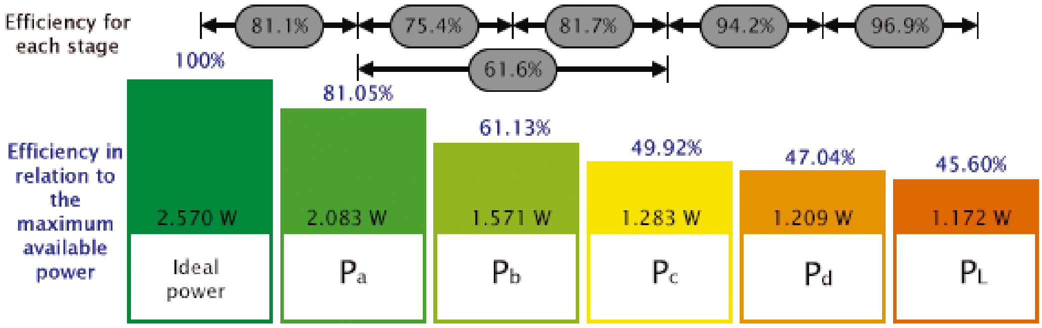

Figure 12. Power flow. P_a, P_b, P_c, P_d, P_L are electric powers that correspond to the notation introduced in Figure 5.

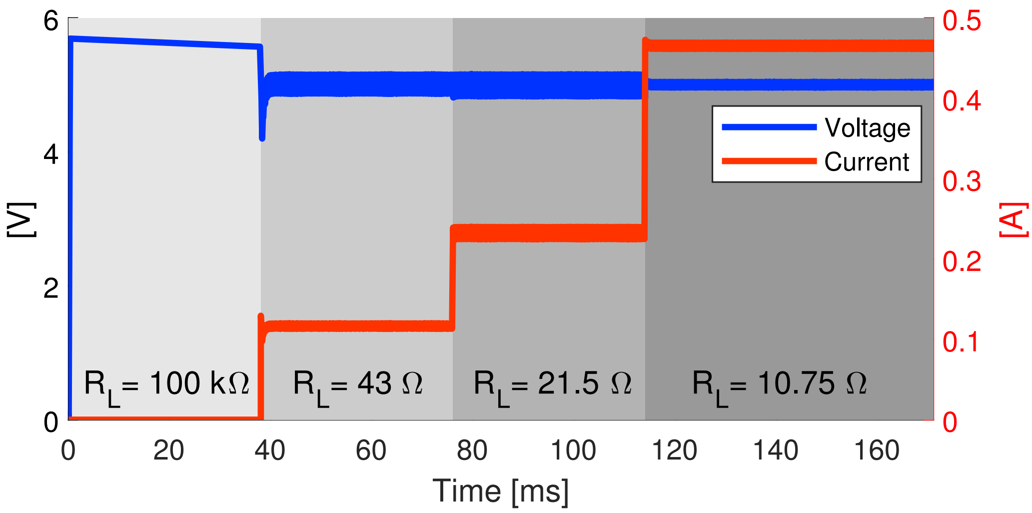

Figure 13. Harvester output voltage and current with different loads.

4.3. Comparison with the State-of-the-Art

The proposed EM harvester is compared to the state of the art in Table 7. As is summarized in the table, there exists a research gap for the development of low-cost EMEH, which could be based on low-cost transceivers (i.e., hub dynamos or two disk generators). Furthermore, the proposed harvester is a cost-effective solution for low-power devices. Another, identified research gap is the lack of standard test conditions, especially in methods related to solving the important question about the mechanical load imposed by the harvester to the bicycle user.

Table 7. Comparison between the proposed EM harvester and the-state-of-the-art.

Harvester	Device	Friction Losses	Electromag. Losses	Electrical Losses	EH Storage Capacity
This Work	Harvester	Low	Low	Medium	Y
Copenhagen Wheel [32]	Byke-Type	N/A***	Medium	Medium	Y
EM Harvester [23]	Transducer	Low	Medium	Medium	N
Hybrid Harvester All [23]	Transducer	Low	Medium	Medium	N
EM Harvester [10]	Transducer	Low	Medium	Medium	N
Hybrid Harvester All [10]	Transducer	Low	Medium	Medium	N
Bottle dynamo [25]	Transducer	High	Low	N/A	N
Hub generator [25]	Transducer	Low	Low	N/A	N
Harvester	**Results**	**Disk Diameter [cm]**	**Output Generate Power [mW]**		**Manufacturing Cost [US]**
This Work	Sim.*	16	1172 @ 225 rpm		83 [a]–299 [b]
Copenhagen Wheel [32]	Exp.**	N/A	N/A		2313 [c]
EM Harvester [23]	Exp.	15	188 @ 3000 rpm		N/A
Hybrid Harvester All [23]	Exp.	15	800 @ 3000 rpm		N/A
EM Harvester [10]	Exp.	15	5.52 @ 160 rpm		N/A
Hybrid Harvester All [10]	Exp.	15	10.07 @ 160 rpm		N/A
Bottle dynamo [25]	Exp.	700C wheel	1200 @ 30 km/h		47.31 [d]
Hub generator [25]	Exp.	700C wheel	4500–6500 @ 30 km/h		50–210 [c]

[a] Components price for one prototype when is manufactured more than a thousand units without a package. [b] Components price for one prototype without package when is manufactured only one. [c] Comercial price. [d] Comercial price with lamp. * Simulated (Sim.).** Experimental (Exp.). *** N/A (Not Available or Not Apply)

5. Conclusions

Mechanical energy harvesting has gained significant attention as a promising approach for powering various electronic devices in self-sustaining systems. In this paper, we explore the use of Halbach arrays on EMEH coupled to a standard bicycle wheel. To evaluate the impact of Halbach arrays on the proposed energy harvester, we conducted simulations using advanced computational models. The simulations were carried out by considering various parameters, including the geometry of the Halbach array, the rotational speed of the bicycle wheel, and the efficiency of electronic converters. The simulated results indicate a substantial enhancement in the performance of the energy harvester when equipped with Halbach arrays, which was a 41.38% of the increase in harvested energy over the same transducer equipped with a standard north-south magnet array. As a result, the proposed harvester generates a simulated output power of 1.17 W with a power processing unit efficiency of 45.6% under a constant bicycle velocity of 30km/h.

Future research will focus on transducer experimental validation and PPU optimization. We expect to be able to improve performance and lower costs by optimizing the PPU (e.g., commercial systems on chip ADP509 or BQ25504). However, the current prototype cost could be competitive with commercial hub dynamos in the near future when it moves from being a prototype to a commercial product.

Author Contributions: Conceptualization, R.U., L.B., J.-P.C., A.F. and G.P.; methodology, R.U., L.B., G.Y., A.F. and G.P.; software, R.U. and L.B.; validation, R.U., L.B., J.-P.C., G.Y. and A.F.; formal analysis, R.U., L.B., J.-P.C., G.Y. and A.F. ; resources, M.P., C.-I.P.-R., G.Y., A.F. and G.P.; writing—original draft preparation, all authors; writing—review and editing, all authors; visualization, R.U., M.P. and A.F.; supervision, M.P., C.-I.P.-R., G.Y., A.F. and G.P.; funding acquisition, M.P., C.-I.P.-R., A.F. and G.P. All authors have read and agreed to the published version of the manuscript.

Funding: The APC was funded by the Pontificia Universidad Javeriana.

Institutional Review Board Statement: Not applicable.

Informed Consent Statement: Not applicable.

Data Availability Statement: The data presented in this study are available on request from the corresponding author.

Acknowledgments: The APC was funded by the Pontificia Universidad Javeriana too. Additionally, the authors would like to thank the Electronics Department and Electronics Laboratory of the Pontificia Universidad Javeriana, for providing the resources required to conduct this study.

Conflicts of Interest: The authors declare no conflict of interest.

References

1. Oliveira, F.; Nery, D.; Costa, D.G.; Silva, I.; Lima, L. A survey of technologies and recent developments for sustainable smart cycling. *Sustainability* **2021**, *13*, 3422. [CrossRef]
2. Hyder, A.A.; Paichadze, N.; Toroyan, T.; Peden, M.M. Monitoring the decade of action for global road safety 2011–2020: An update. *Glob. Public Health* **2017**, *12*, 1492–1505. [CrossRef] [PubMed]
3. Koszowski, C.; Gerike, R.; Hubrich, S.; Götschi, T.; Pohle, M.; Wittwer, R. Active mobility: Bringing together transport planning, urban planning, and public health. In *Towards User-Centric Transport in Europe: Challenges, Solutions and Collaborations*; Springer: Berlin/Heidelberg, Germany, 2019; pp. 149–171.
4. Kim, J.; Choi, K.; Kim, S.; Fujii, S. How to promote sustainable public bike system from a psychological perspective? *Int. J. Sustain. Transp.* **2017**, *11*, 272–281. [CrossRef]
5. Schwanen, T. Beyond instrument: Smartphone app and sustainable mobility. *Eur. J. Transp. Infrastruct. Res.* **2015**, *15*. [CrossRef]
6. Yang, F.; Ding, F.; Qu, X.; Ran, B. Estimating urban shared-bike trips with location-based social networking data. *Sustainability* **2019**, *11*, 3220. [CrossRef]
7. Chang, Y.N.; Cheng, H.L.; Chan, S.Y.; Huang, L.H. Electromagnetic energy harvester and energy storage system for bike lighting applications. *Sens. Mater.* **2018**, *30*, 1341–1347. [CrossRef]
8. Abu-Rayash, A.; Dincer, I. Development and analysis of an integrated solar energy system for smart cities. *Sustain. Energy Technol. Assess.* **2021**, *46*, 101170. [CrossRef]
9. Jaimes, A.F.; deSousa, F.R. Modeling and design of high-efficiency power amplifiers fed by limited power sources. In Proceedings of the 2016 29th Symposium on Integrated Circuits and Systems Design (SBCCI), Belo Horizonte, Brazil, 29 August–3 September 2016 ; IEEE: Piscataway, NJ, USA, 2016; pp. 1–6.
10. Dai, X.; Wang, H.; Wu, H.; Pan, Y.; Luo, D.; Ahmed, A.; Zhang, Z. A hybrid energy harvesting system for self-powered applications in shared bicycles. *Sustain. Energy Technol. Assess.* **2022**, *51*,101891. [CrossRef]
11. Enayati, J.; Asef, P. Review and analysis of magnetic energy harvesters: A case study for vehicular applications. *IEEE Access* **2022**, *10*, 79444–79457. [CrossRef]
12. FajardoJaimes, A. Contributions on the Energy Flow Modeling in a Self-Sustainable Wireless Energy Transfer System Based on Efficient Inductive Links. Ph.D. Thesis, Federal University of Santa Catarina, Florianopolis, Brazil, 2017.
13. Kansal, A.; Hsu, J.; Zahedi, S.; Srivastava, M.B. Power management in energy harvesting sensor networks. *Acm Trans. Embed. Comput. Syst. (Tecs)* **2007**, *6*, 32-es. [CrossRef]
14. Priya, S.; Inman, D.J. *Energy Harvesting Technologies*; Springer: Berlin/Heidelberg, Germany, 2009; Volume 21.
15. Doria, A.; Marconi, E.; Moro, F. Energy harvesting from bicycle vibrations. *IEEE Trans. Ind. Appl.* **2021**, *57*, 6417–6426. [CrossRef]
16. Chen, P.; Yang, Y. Design, Dynamics Modeling, and Experiments of a Vibration Energy Harvester on Bicycle. *IEEE/Asme Trans. Mechatron.* **2023**. [CrossRef]
17. Yang, Y.; Yeo, J.; Priya, S. Harvesting energy from the counterbalancing (weaving) movement in bicycle riding. *Sensors* **2012**, *12*, 10248–10258. [CrossRef] [PubMed]
18. Vasic, D.; Chen, Y.Y.; Costa, F. Self-powered piezoelectric energy harvester for bicycle. *J. Mech. Sci. Technol.* **2014**, *28*, 2501–2510. [CrossRef]
19. Zhou, H.; Liu, G.; Gao, Y.; Wang, Z.; Qin, Y.; Wang, Y.; Lin, Y.; Xie, Y.; Chen, Y.; Zhang, C. Dual mode rotary triboelectric nanogenerator for collecting kinetic energy from bicycle brake. *Adv. Energy Sustain. Res.* **2021**, *2*, 2000113. [CrossRef]
20. Nazar, A.M.; Narazaki, Y.; Rayegani, A.; Sardo, F.R. Recent progress of triboelectric nanogenerators as self-powered sensors in transportation engineering. *Measurement* **2022**, *23*, 112010. [CrossRef]
21. Leng, Q.; Guo, H.; He, X.; Liu, G.; Kang, Y.; Hu, C.; Xi, Y. Flexible interdigital-electrodes-based triboelectric generators for harvesting sliding and rotating mechanical energy. *J. Mater. Chem.* **2014**, *2*, 19427–19434. [CrossRef]
22. Pan, H.; Qi, L.; Zhang, Z.; Yan, J. Kinetic energy harvesting technologies for applications in land transportation: A comprehensive review. *Appl. Energy* **2021**, *286*, 116518. [CrossRef]
23. Wang, X.; Wang, Z.L.; Yang, Y. Hybridized nanogenerator for simultaneously scavenging mechanical and thermal energies by electromagnetic-triboelectric-thermoelectric effects. *Nano Energy* **2016**, *26*, 164–171. [CrossRef]

24. Zhang, C.; Tang, W.; Han, C.; Fan, F.; Wang, Z.L. Theoretical comparison, equivalent transformation, and conjunction operations of electromagnetic induction generator and triboelectric nanogenerator for harvesting mechanical energy. *Adv. Mater.* **2014**, *26*, 3580–3591. [CrossRef]
25. Heine, J.; Oehler, A. Testing the efficiency of generator hubs. *Vintage Bicycl. Q.* **2005**, *3*, 27–30.
26. Kumar, V.; Verma, D.P. Design and fabrication of planetary drive magnet pedal power hub-dynamo. *Adv. Mater. Sci. Eng. Int. J. (MSEJ)* **2015**, *2*, 105–107. [CrossRef]
27. Brito, N.; Ribeiro, L.; Esteves, J.S. Electric power generating bicycle. In Proceedings of the International Conference on Hands on Science, Braga, Portugal, 4–9 September 2006; pp. 1–6, ISBN 989-9509-50-7.
28. Lillington, A. The Rechargalite: A different concept in bicycle illumination. *Electron. Educ.* **1991**, *1991*, 17–18. [CrossRef]
29. Kothari, D.G.; Patel, J.C.; Panchal, B.R.; Goswami, H. Hybrid Bicycle. *IJEDR* **2014**, *2*, 585–588.
30. Suhalka, R.; Khandelwal, M.C.; Sharma, K.K.; Sanghi, A. Generation of electrical power using bicycle pedal. *Int. J. Recent Res. Rev.* **2014**, *7*, 63–67.
31. Jadhav, M.K.; Jadhav, S.A.; Kate, A.A.; Gholap, S.G. Design and analysis of hub dynamo for electric vehicle. In Proceedings of the 2018 International Conference On Advances in Communication and Computing Technology (ICACCT), Sangamner, India, 8–9 February 2018; IEEE: Piscataway, NJ, USA, 2018; pp. 262–264.
32. Superpedestrian Copenhagen Wheel Review. Available online: https://electricbikereview.com/superpedestrian/copenhagen-wheel/ (accessed on 21 May 2023).
33. Salauddin, M.; Rasel, M.; Kim, J.; Park, J.Y. Design and experiment of hybridized electromagnetic-triboelectric energy harvester using Halbach magnet array from handshaking vibration. *Energy Convers. Manag.* **2017**, *153*, 1–11. [CrossRef]
34. Ma, C.; Zhao, W.; Qu, L. Design optimization of a linear generator with dual Halbach array for human motion energy harvesting. In Proceedings of the 2015 IEEE International Electric Machines & Drives Conference (IEMDC), Coeur d'Alene, ID, USA, 10–13 May 2015; IEEE: Piscataway, NJ, USA, 2015; pp. 703–708.
35. Sajwani, H.; AlSuwaidi, N.; Elshikh, M.; AlJaberi, A.; Meribout, M. Hallbach array-based linear generator for human motion energy harvesting. In Proceedings of the 2017 International Conference on Electrical and Computing Technologies and Applications (ICECTA), Ras Al Khaimah, United Arab Emirates, 21–23 November 2017; IEEE: Piscataway, NJ, USA, 2017; pp. 1–6.
36. Li, Z.; Yan, Z.; Luo, J.; Yang, Z. Performance comparison of electromagnetic energy harvesters based on magnet arrays of alternating polarity and configuration. *Energy Convers. Manag.* **2019**, *179*, 132–140. [CrossRef]
37. Liu, X.; Qiu, J.; Chen, H.; Xu, X.; Wen, Y.; Li, P. Design and optimization of an electromagnetic vibration energy harvester using dual Halbach arrays. *IEEE Trans. Magn.* **2015**, *51*, 1–4. [CrossRef]
38. Qiu, J.; Liu, X.; Hu, Z.; Chang, Q.; Gao, Y.; Yang, J.; Wen, J.; Tang, X.; Hu, W. Multi-directional electromagnetic vibration energy harvester using circular Halbach array. *AIP Adv.* **2017**, *7*, 056672. [CrossRef]
39. Kim, J.W.; Salauddin, M.; Cho, H.; Rasel, M.S.; Park, J.Y. Electromagnetic energy harvester based on a finger trigger rotational gear module and an array of disc Halbach magnets. *Appl. Energy* **2019**, *250*, 776–785. [CrossRef]
40. Magnets/Neodymium Iron Boron Magnets Datasheet. Available online: https://www.eclipsemagnetics.com/site/assets/files/19485/ndfeb_neodymium_iron_boron-standard_ndfeb_range_datasheet_rev1.pdf (accessed on 21 May 2023).
41. Superimanes. Available online: https://www.superimanes.com/ (accessed on 21 May 2023).
42. Semiconductor Components Industries LLC. Datasheet MBRS410L Surface Mount Schottky Power Rectifier. Available online: https://www.onsemi.com/pdf/datasheet/mbrs410lt3-d.pdf (accessed on 21 May 2023).
43. Datasheet 160 MHz Rail-to-Rail Amplifier AD8041. Available online: https://www.analog.com/media/en/technical-documentation/data-sheets/AD8041.pdf (accessed on 21 May 2023).
44. Datasheet TPS61288. Available online: https://www.ti.com/product/TPS61288 (accessed on 21 May 2023).
45. PowerPoint Presentation. Available online: https://courses.ansys.com/wp-content/uploads/2021/07/MAXW_GS_2020R2_EN_LE03.pdf (accessed on 21 May 2023).
46. PSpice User Guide—PSpice User Guide. Available online: https://resources.pcb.cadence.com/i/1180526-pspice-user-guide/852? (accessed on 21 May 2023).